



UNIVERSIDAD DE SONORA

DIVISIÓN DE CIENCIAS EXACTAS Y NATURALES

Departamento de Investigación en Física

Computational Modelling of Nanoalloys

TESIS DE MAESTRÍA

Que para obtener el grado de:

Maestro en Ciencias (Física)

Presenta:

Josafat Guerrero Jordan

Director(es):

Prof. Roy L. Johnston
Dr. Alvaro Posada Amarillas

Hermosillo, Sonora, México

21 de diciembre de 2012

Universidad de Sonora

Repositorio Institucional UNISON



**"El saber de mis hijos
hará mi grandeza"**



Excepto si se señala otra cosa, la licencia del ítem se describe como openAccess

SINODALES

Dr. Alvaro Posada Amarillas
Universidad de Sonora. Hermosillo, México.

Dr. Marcelino Barboza Flores
Universidad de Sonora. Hermosillo, México.

Dr. Jorge Alberto Gaspar Armenta
Universidad de Sonora. Hermosillo, México.

Dr. Ronaldo Herrera Urbina
Universidad de Sonora. Hermosillo, México.

AGRADECIMIENTOS

A mi familia

Por el apoyo incondicional en mi carrera profesional y mi vida personal.

A mis amigos

Por darme el impulso necesario para que este día llegara.

A mis maestros

Por iluminar el mundo.

A mis directores

Alvaro Posada y Roy Johnston por hacer conmigo este gran trabajo.

A la Universidad de Sonora

Por las herramientas que permiten el desarrollo de tantos profesionales.

A CONACYT

Por financiar este sueño.

CONTENTS

SINODALES	2
AGRADECIMIENTOS	3
LIST OF FIGURES	7
LIST OF TABLES	9
ABBREVIATIONS AND SYMBOLS	10
1. INTRODUCTION	11
2. EXPERIMENTAL AND THEORETICAL BACKGROUND	13
2.1 Synthesis and cluster characterization	13
2.2 The transmission electron microscope	15
2.2.1 STEM Simulation	17
2.3 Nanoalloys	18
2.3.1 Homotops	18
2.4.2 Segregation in nanoalloys	19
2.3.2.1 Segregated configurations	20
2.4.1 Cu monometallic properties	21
2.4.2 Pt monometallic properties	21
2.4.3 Comparison of Cu and Pt monometallic clusters	22
2.4.4 Cu-Pt bimetallic properties	22
2.5 Genetic algorithms and the optimization of cluster geometries	26

2.6. DFT	28
3. COMPUTATIONAL METHODOLOGY	31
3.1 The Gupta Potential	31
3.1.1 Parameterization of the Gupta Potential	32
3.2 The Birmingham Cluster Genetic Algorithm	34
3.3 Energetic Analysis	38
3.4 Chemical Ordering	38
3.5 Density Functional Theory	39
3.6 Pair Distribution Function	39
4. RESULTS AND DISCUSSION	41
4.1 BCGA Structures	41
4.2 Excess Energy	42
4.3 TO vs iMplh, energy comparison.	43
4.4 Chemical Ordering	44
4.5 Density Functional Theory and Average Nearest Neighbor Distance	45
4.6 Scanning transmission electron microscopy	47
5. CONCLUSIONS	49
REFERENCES	50

LIST OF FIGURES

<i>Figure 1.</i> Experiments under collision-free conditions.	11
<i>Figure 2.</i> Electron microscopy images of supported nanoalloys.	12
<i>Figure 3.</i> Comparison of CTEM and STEM.	13
<i>Figure 4.</i> Different segregation arrangements found in nanoalloys.	17
<i>Figure 5.</i> The vibrational C-O stretching frequency of M ₂ -CO transition metalcarbonyl clusters.	20
<i>Figure 6.</i> Experimental and calculated CO adsorption energies on transition metal clusters.	20
<i>Figure 7.</i> The H binding energy and CO binding energy of various transition metal nanoalloys.	21
<i>Figure 8.</i> The solid-solid phase equilibria of CuPt.	22
<i>Figure 9.</i> Schematic representation of the crossover operation in a generic GA.	25
<i>Figure 10.</i> Flow chart for the BCGA program.	28
<i>Figure 11.</i> Schematic representation of the Deaven–Ho cut and splice crossover operation, as implemented in our GA program.	30
<i>Figure 12.</i> Structure map for all weightings and compositions.	41
<i>Figure 13.</i> Three remarkable structures.	42
<i>Figure 14.</i> Excess energy for all weightings and compositions.	43
<i>Figure 15.</i> Energy comparison between iMplh and TO.	43

<i>Figure 16.</i> Mixing layouts.	44
<i>Figure 17.</i> Number of bonds per composition.	45
<i>Figure 18.</i> Comparison after DFT optimization.	46
<i>Figure 19.</i> ANND of $\text{Cu}_{32}\text{Pt}_6$ before and after DFT reoptimization.	47
<i>Figure 20.</i> STEM simulation of $\text{Cu}_{32}\text{Pt}_6$.	48

LIST OF TABLES

<i>Table 1.</i> Some image simulation software packages appearing in the literature or on-line.	16
<i>Table 2.</i> CuPt crystal structures and lattice parameters.	23
<i>Table 3.</i> Gupta potential parameters.	36
<i>Table 4.</i> Parameter set values.	37

ABBREVIATIONS AND SYMBOLS

1D-LPS. One-Dimensional Long Period Structure.	PVP. Polyvinylpyrrolidone.
ADF. Annular Dark Field.	PW91. Perdew-Wang 1991
AFM. Atomic Force Microscopy.	SA. Simulated Annealing.
ANND. Average Nearest Neighbor Distance.	STEM. Scanning Transmission Electron Microscope.
BCGA. Birmingham Cluster Genetic Algorithm.	TEM. Transmission Electron Microscope.
BF. Bright Field.	TO. Truncated Octahedron.
CPU. Computer Processing Unit.	XANES. X-ray Absorption Near Edge Structure.
CTEM. Conventional Transmission Electron Microscope.	XAS. X-ray Absorption Spectroscopy
DFT. Density Functional Theory.	
Dh. Decahedron.	
DNA. Deoxyribonucleic Acid	
EXAFS. Extended X-ray Absorption Fine Structure.	
FFT. Fast Fourier Transform.	
GA. Genetic Algorithm.	
GGA. Generalized Gradient Approximation.	
GM. Global Minimum.	
HAADF. High Angle Annular Dark Field.	
HRTEM. High Resolution Transmission Electron Microscope.	
iaMpIh. Incomplete anti-Mackay poli-Icosahedron.	
iMpIh. Incomplete Mackay poli-Icosahedron.	nm. nanometer
L-BFGS. Limited-memory Broyden-Fletcher-Goldfarb-Shanno	Å. angstrom
LDA. Local Density Approximation	eV. electronvolt
MC. Monte Carlo.	cm. centimeter
MD. Molecular Dynamics.	kcal. kilocalorie
NSA. Near Surface Alloy.	K. kelvin
PDF. Pair Distribution Function.	a.u. atomic units

1. INTRODUCTION

The physical and chemical properties of nanoparticles are completely different from those of crystalline bulk solids, strongly varying as a function of size, shape, chemical ordering and composition [1]. We now know that the bonding in a small metal or semiconductor cluster is different from that in the bulk. An atom at the surface of a large portion of material is different from the atom of the same element inside that portion. Additionally, an atom at the smooth surface of a sizable single crystal is different from an atom at the surface of a small cluster of the same element. Moreover, the properties of a surface atom of a small metal cluster depend on the type of support on which it is deposited or whether the cluster is doped with one or a few atoms of a different element [2].

There are basically two types of size-dependent effects which dictate the great variety of properties present in nanoparticles: those smoothly scalable which are related to the fraction of atoms in the surface, and quantum effects that show a discontinuous behavior due to the completion of electronic shells on systems with delocalized electrons [3].

At present, large-scale scientific research focuses on the fabrication, manipulation, visualization and modeling of metallic systems on the nanometer scale (1×10^{-9} m). The concept of nanoscience or nanotechnology was initially expressed in the early 1960's, by the famous American scientist Richard Feynman. In one of his lectures at Caltech, he asked the question "how small we can go in the process of miniaturization" [4]. He was fascinated by how biological systems, while being so small, are capable of storing such an enormous amount of information (e.g. the genetic information encoded in DNA). He challenged scientists to develop new technologies which could allow the construction and manipulation, at the atomic level, of devices comprising up to a few hundred atoms. Impressive progress has recently been achieved in this field thanks to the development of atomic structure theories, experimental microscopy techniques and the development of new and powerful computational technologies such as massively parallel supercomputing and distributed grid computing. The combination of theoretical methodologies and computational tools have proved to be an efficient way for tackling scientific problems related to nanometer scale systems [5,6].

The main goal of this work is to understand the structural evolution of bimetallic Cu-Pt nanoparticles as a function of their chemical composition and characterize them by DFT methods. The general objectives of this research were:

- To understand the structural evolution of bimetallic Cu-Pt nanoparticles as a function of chemical composition.
- Use DFT calculations to make a reoptimization of selected structures obtained using empirical potentials and BCGA to make comparisons.

2. EXPERIMENTAL AND THEORETICAL BACKGROUND

2.1 Synthesis and cluster characterization

The outline of the experimental production (synthesis) and characterization (visualization) of nanoparticles becomes important, despite this work has only focused on the computational modeling of nanoalloys. One of the most commonly known ways for the synthesis of gas-phase clusters is the so-called cluster molecular beam (see Figure 1).

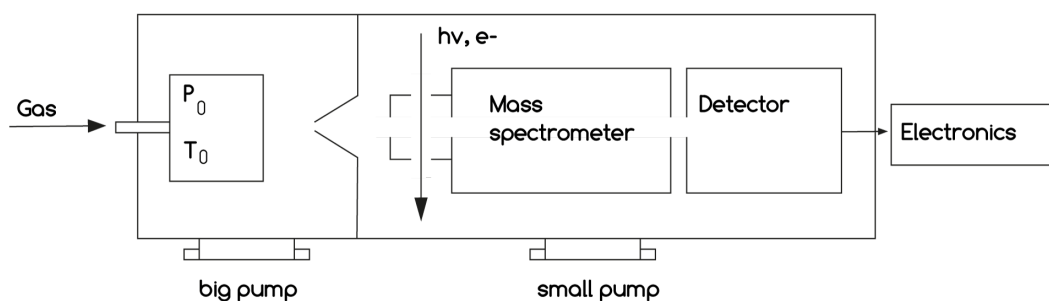


Figure 1. Experiments under collision-free conditions [18].

The first step in the experimental production of this type of nanoparticle involves the evaporation of bulk material in the plate or rod by laser ablation [19]. When producing bimetallic nanoalloys, a single metal may be used, or two pure metals. Evaporation can also be performed by heavy ion sputtering, magnetron sputtering or electrical discharge. This process generates a plasma which is then cooled down via collisions with a cold gas (helium or argon), which in turn results in condensation and cluster nucleation. Clusters are grown by collisions. Strong cooling takes place due to adiabatic and isenthalpic expansion, as the clusters undergo a supersonic expansion when passing from the high-pressure condensation region through a narrow nozzle into a vacuum. There are no collisions within the supersonic jet and the characteristics of isolated clusters can be easily investigated (see figure 2) [6,18,19].

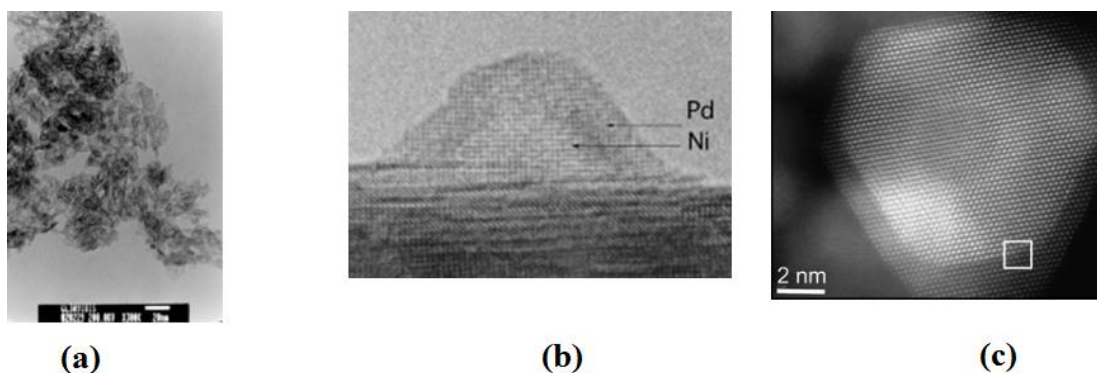


Figure 2. Electron microscopy images of supported nanoalloys. (a) TEM image of Pd₆Pt catalyst (~ 6 nm), (b) HRTEM image of Ni-Pd nanoparticles (~ 3 nm) and (c) HAADF-STEM image of a three-layer cuboctahedral Pd-Au nanoparticle (~ 12 nm) [20,21,22].

Chemical techniques for cluster production also include chemical reduction, in which clusters are generated by reduction of different metal salt solutions in the presence of surfactant. Particle size can be controlled by the use of inverse micelles. Electrochemical synthesis involves the generation of metals such as Pt, Rh and Ru by reducing of their corresponding salts at the cathode [6].

Mass spectrometry is an experimental technique used for cluster characterization. This method allows the ionization of the cluster which in turn is deflected by an applied electric field. By changing the intensity of the electric field, cluster mass can be selected, i.e. cluster particle size. X-ray diffraction can determine the structure and crystallinity of the cluster. Z-contrast HAADF-STEM is able to reveal the internal structure of the nanoparticle. Topography of the nanoparticle can be obtained by AFM. XAS and EXAFS are both based on the fact that each element has a unique X-ray absorption spectrum [23].

It becomes evident that the appropriate combination of computational and theoretical methods, especially modeling of nanoparticles, with experimental techniques will lead to a thorough understanding of the physicochemical properties of nanoparticles.

2.2 The transmission electron microscope

There are two fundamental forms of TEM as is illustrated in a simplified schematic form in figure 3. In the conventional or fixed beam form (CTEM) the specimen is illuminated by a parallel (or nearly so) beam of electrons. An objective lens forms an image of the specimen in parallel with a fixed beam similar to a standard light optical microscope. The bright field image is typically phase contrast. In the scanning form (STEM) a small focused probe (of order 1 to 2 Å in diameter) is scanned across the specimen in raster form. The transmitted electrons that have been scattered to large angles form an ADF image that has a strong dependence on the atomic number of the atoms in the specimen (Z-contrast). The transmitted electrons that are on the optic axis form the BF image which exhibits phase contrast similar to CTEM.

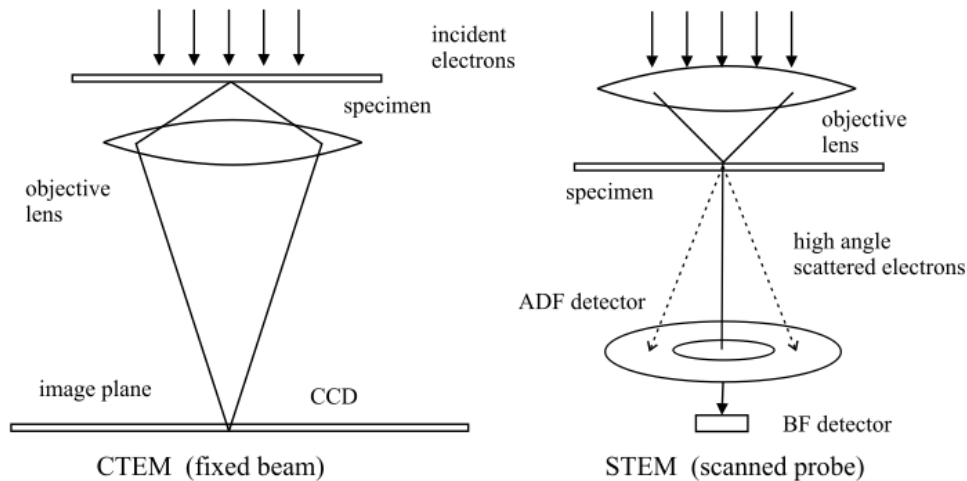


Figure 3. Comparison of CTEM and STEM. Simplified schematic of the CTEM (left) and the STEM (right) [24].

There are a large number of things that can go wrong in an image simulation. The proposed specimen structure must be specified in some detail, usually in the form of a list of atomic coordinates and atomic numbers in a unit cell. Even less well known is the thickness of the specimen. Usually a large sequence of possible specimen thicknesses are calculated and compared to experiment.

The instrumental (optical) parameters such as the aberration constants (spherical aberration constant, etc.) and aperture size of the objective lens and lens defocus must be known. Usually defocus is not known very well (particularly in bright field phase contrast). Frequently a defocus series is calculated for comparison to experiment. There are also a variety of parameters such as defocus spread, illumination angle etc. that are hard to estimate but can influence the image [24].

There are also many parameters that are solely related to the calculation and have very little to do with the microscope or specimen but can dramatically affect the calculation. These parameters include the sampling size (pixel size) in the image and slices and the slice thickness itself.

Multi-slice almost always uses an FFT to reduce the total CPU time. The FFT is a discrete Fourier transform which repeats the image infinitely in all directions. Although the image is only displayed as a single image one should remember that it is really an infinite array of identical side-by-side images. This produces a strange effect called the wrap-around error. The left side of the image in essence touches the right side of the image (and vice versa) and the top of the image touches the bottom of the image (see fig. 6.10 and 6.11 in reference 24). To use the FFT each image and slice must obey periodic boundary conditions or be an integer number unit cells of the specimen (called a super cell). Interfaces and defects must be embedded inside a large super cell (brief discussion in section 6.8 of reference 24).

In summary, some of the things that need to be specified correctly are:

- Specimen parameters: atomic coordinates and numbers of the specimen and thickness of specimen
- Instrumental parameters: defocus, Cs, objective aperture, etc.
- Sampling size: number of pixels in the image and slice and the slice thickness. Ensure that the total integrated intensity is at least 0.9 or higher (1.0 to start). Calculations with slightly higher or lower sampling should yield the same result if the sampling is adequate.
- Slice thickness: usually the slices should correspond to the existing atomic layers in the specimen.

2.2.1 STEM Simulation

Computer simulation of images has become a routine tool of high-resolution transmission electron microscopy (conventional and scanning) of materials. The resolution of high resolution CTEM or STEM graphs of materials are primarily limited by the aberrations of the lenses in the microscope and multiple scattering in the specimen [25].

Even for very thin specimens, the imaging electrons will likely interact strongly enough with the specimen to be scattered more than once while traveling through the specimen. This multiple scattering may influence the image in unexpected ways such that the image is no longer related to the specimen structure in a simple manner. The goal of image simulation is to understand this image structure better. In summary the main goals of image simulation are:

Understanding: Image simulation may help to understand the detailed structure in the image to separate what is due to the specimen, what is due to the instrument and to help unravel the effects of multiple scattering.

Improvement: Image simulation may help to understand how the image is formed and generate intuition on ways to improve the image and instrumentation [24].

There are a variety of image calculation programs in existence. Many have been written for private use only. Some have been made available commercially and some are available as a free download. A partial list of some programs is shown in table 1.

Table 1. Some image simulation software packages appearing in the literature or on-line. Type M is multi-slice and type B is Bloch-Wave. Some of the listed programs may be commercial. Many other private programs likely exist [24].

Program	Author	Year
SHRLI	O'Keefe and Buseck	1978
TEMPAS	Kilaas	1987
EMS	Stadelmann	1987
NCEMSS	O'Keefe and Kilaas	1988
TEMSIM	Kirkland	1998
JEMS	Stadelmann	2004
WebEMAPS	Zuo	2005
HAADF-STEM	Logsdail, Li and Johnston	2012

2.3 Nanoalloys

Metallic nanoparticles have been the subject of study for around three decades, while only during the past fifteen years there has been a boom in the interest in bi- and multimetallic clusters, known as nanoalloys. Nanoalloys are unique materials with special characteristics, as they represent a type of finite-size objects. By controlling the size, composition and degree of chemical ordering (degree of mixing) [1,5,6,7,8] the chemical and physical properties of these novel materials can be modified. Catalytic conversion in the treatment of exhaust gases (e.g. CO) represents one of the main industrial applications of metal nanoparticles and nanoalloys. These gases are generated as products of incomplete combustion in car engines and other industrial processes, contributing to air pollution, acid rain and global warming effects.

2.3.1 Homotops

The term *homotop* was coined by Julius Jellinek [8,9] to describe alloy cluster isomers (A_mB_n) with a fixed number of atoms ($N = m+n$) and composition (m/n ratio) that is the case of bimetallic nanoalloys (e.g. Pd-Pt, Pd-Au, Ag-Pt, Cu-Pt, Ag-Au). These isomers possess the same

geometrical disposition of their atoms but differ in the way in which A and B type atoms are arranged. The number of homotops is defined by the next expression:

$$N_H = \frac{N!}{N_A!N_B!} = \frac{N!}{N_A!(N - N_A)!}$$

N_H is maximum when $N_A = N_B$, in other words for the 50:50 mixture. Therefore, the number of homotops increases combinatorially, making the global optimization search a difficult endeavor.

2.4.2 Segregation in nanoalloys

The chemical ordering of the atoms A (in red) and B (in yellow) within the nanoalloy structure will create a characteristic mixing pattern. Figure 4 shows different possible ways in which these two types of atoms can be arranged, according to mixed or segregated behavior.

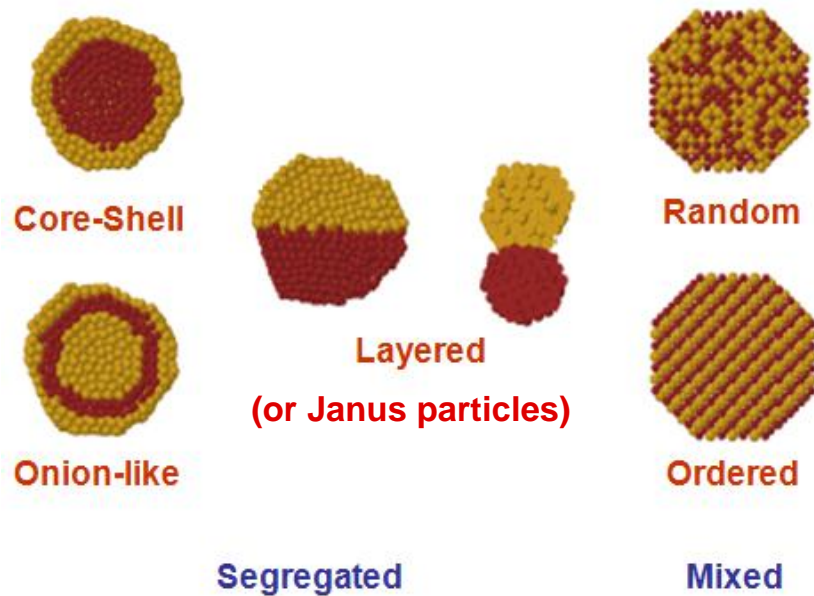


Figure 4. Different segregation arrangements found in nanoalloys [6].

2.3.2.1 Segregated configurations

Segregation in bimetallic nanoalloys can be found in different arrangement of atoms:

- *Core-shell*: One element (A) occupies core positions in the nanoparticle, while a shell, created of B atoms, completely surrounds the core.
- *Onion-like*: Usually found in medium-large clusters, in which clusters present a layered A-B-A alternating shell pattern.
- *Layered*: These structures (aka. Janus particles) minimize the number of A-B bonds. They are in contact only at a small interface.
- *Random mixing*: The so called “alloyed” nanoparticles possess randomly mixed patterns, corresponding to bulk solid solutions.
- *Ordered mixing*: Pseudo-crystalline regular arrangements of A-B atoms.

The type of segregation present on a specific nanoalloy depends on many factors such as:

- Bond strength. This relates to the relative strengths of A-A, B-B and A-B bonds between metal atoms. If the homonuclear bonds are stronger segregation is preferred, while stronger A-B bonds will favor mixing.
- Surface energy. The metal with the lowest surface energy will segregate to nanoparticle surface sites.
- Atomic size. This is related to the release of strain effects in the nanoparticle itself, with the smaller atom tending to occupy core positions.
- Charge transfer. This means that the most electronegative atom will tend to occupy surface sites.
- Strength of binding to ligands. The metal which binds more strongly to the ligand will prefer to occupy surface sites (especially true for passivated clusters).
- Specific electronic effects. For certain metals, specific electronic effects may play an important role in determining segregation.

For a given size and composition for a specific nanoalloy, in terms of their geometrical disposition and chemical ordering and electronic structure, a problem arises when trying to determine the most stable cluster (GM) [10-17]. Once this issue is cleared up, structure-property relations can be investigated.

2.4.1 Cu monometallic properties

Copper nanoparticles play an important role in several relevant technological applications, for example in metallurgical and petrochemical applications, being significant in automobile exhaust purification as a substitute for the more expensive transition metal (Pt and Ru) components of catalytic converters. Carbon monoxide (CO) chemisorption on high purity copper has been the subject of several investigations. There are reports showing that CO adsorption takes place on top of the three fold Cu(111) hollow and Cu(001) bridge-sites. For the Cu(111) hollow, the C-O bond stretching frequency of the CO changes upon adsorption from 2145 cm^{-1} to 2070 cm^{-1} [26]. It is observed that as the coordination number of Cu increases the Cu-CO bond also increases. On the other hand, during Cu-CO bonding, the inward relaxation of the top layer and the buckling amplitudes are reduced. Spin unrestricted DFT has been used to predict the most stable spin multiplicity for $\text{Cu}_2\text{-CO}$ [27]. This spin multiplicity was found to be $2S + 1 = 1$ (singlet). The vibrational stretching frequency of CO is 2161 cm^{-1} and the adsorption energy of the Cu-CO is 17.2 kcal/mol , which is in agreement with the experimental value reported by Zeinalipour et al [27]. The latter researchers also showed that $\text{Cu}_4\text{-CO}$ clusters relax into a planar structure with C_s symmetry.

2.4.2 Pt monometallic properties

Platinum (Pt) makes an excellent catalyst when used as an anode in pure H_2 in fuel cells. The presence of CO in the mixture, however makes Pt unsuitable because it binds strongly to the metal when its concentration is 20 ppm or higher. Pt (111) shows a theoretical adsorption energy of CO-Pt of -1.39 eV (experimental value: -1.49 eV) when binding to the top Pt sites [28].

2.4.3 Comparison of Cu and Pt monometallic clusters

The correlation between transition metals and vibrational frequencies of the CO bonding stretching (V_{CO}) adsorption is shown on Figure 5. For Cu_2-CO the bridging C-O stretching frequency is higher at around 2115 cm^{-1} than Pt_2-CO which is around 2090 cm^{-1} . The increasing population of the d-shell of any given quantum number, n , significantly augments the adsorption energies of CO (see figure 6). In this case, Cu_2-CO adsorption energy has a value of around 18 kcal/mol lower than that for Pt (42 kcal/mol). This means that Cu binds more weakly to CO, reducing the chance of Pt poisoning in the bimetallic alloy [29].

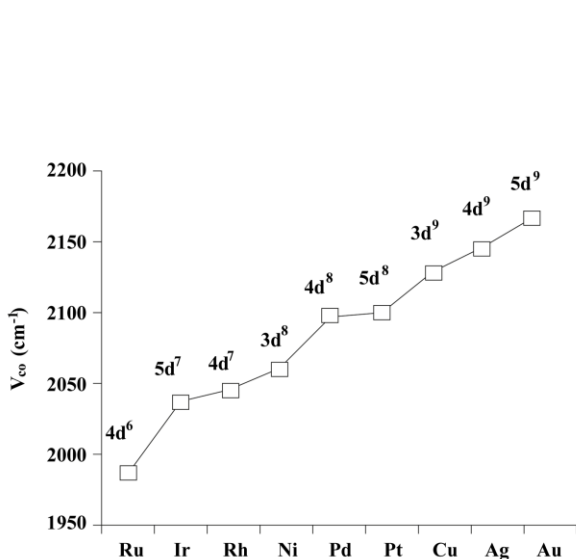


Figure 5. The vibrational C-O stretching frequency of M_2-CO transition metalcarbonyl clusters [27].

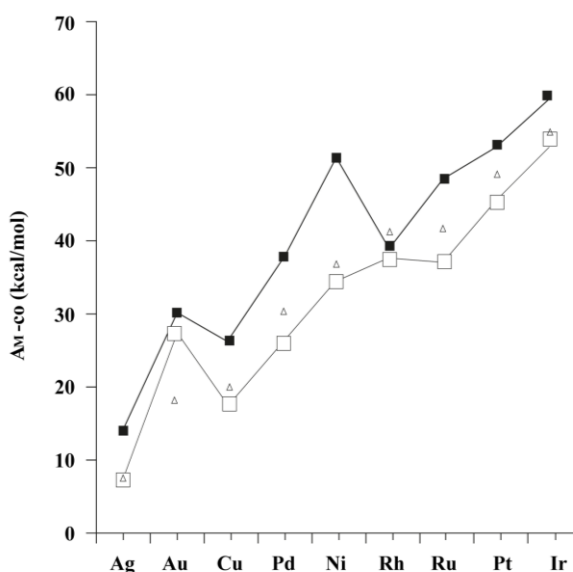


Figure 6. Experimental and calculated CO adsorption energies on transition metal clusters. The open white squares represent M_2-CO , the solid squares represent M_4-CO and the triangles represent experimental values [27].

2.4.4 Cu-Pt bimetallic properties

Differences in Cu-Pt alloys come about due to the fact that Cu is a third-row quasi-noble metal and Pt is a fifth-row noble metal. Another notable distinction is electronegativity, $Pt = 2.28$, $Cu = 1.90$, which explains Pt's propensity to attract electrons towards it.

The synthesis of Cu-Pt nanoclusters includes a variety of methods [30,31,32]. One of these procedures includes the immersion of the CuPt in a solution of glycol and water in the presence of PVP. This is a reduction method. When formed experimentally, Cu-Pt clusters contain different molar ratios, possess fcc structure [33], are spherical, elongated [34] and have a mean particle size of 8 nm [6]. Cu-Pt NSAs could potentially facilitate highly selective hydrogenation reactions at low temperatures. The use of Cu-Pt NSAs facilitates H₂ dissociation due to the weak atomic hydrogen bonding [36]. This makes Cu-Pt nanoalloys good potential anodes in fuel cells. Computational studies of Cu-Pt nanoparticles have used structures with symmetries C_{3v}, D_{2d}, D_{4h}. The absorption of ethylene in Cu₁₂Pt₂ clusters has been investigated [35]. The relative stability of the different isomeric structures follows the order: C_{3v}>D_{2d}>D_{4h} [34]. One of the reasons for this addition of Pt to Cu is because it modifies the valence spd-band of the cluster improving its catalytic characteristics [36].

The existence of a linear correlation between near-surface transition metal alloys and H and CO binding energies has been proved. This is shown in Figure 7. In the diagram, Cu/Pt is in the middle with a CO binding energy of around -1.5eV and a H binding energy of around -2.75 eV. This means H bonding and CO bonding are both in the middle of the range and so neither is strongly preferred, therefore both association and dissociation can take place [28].

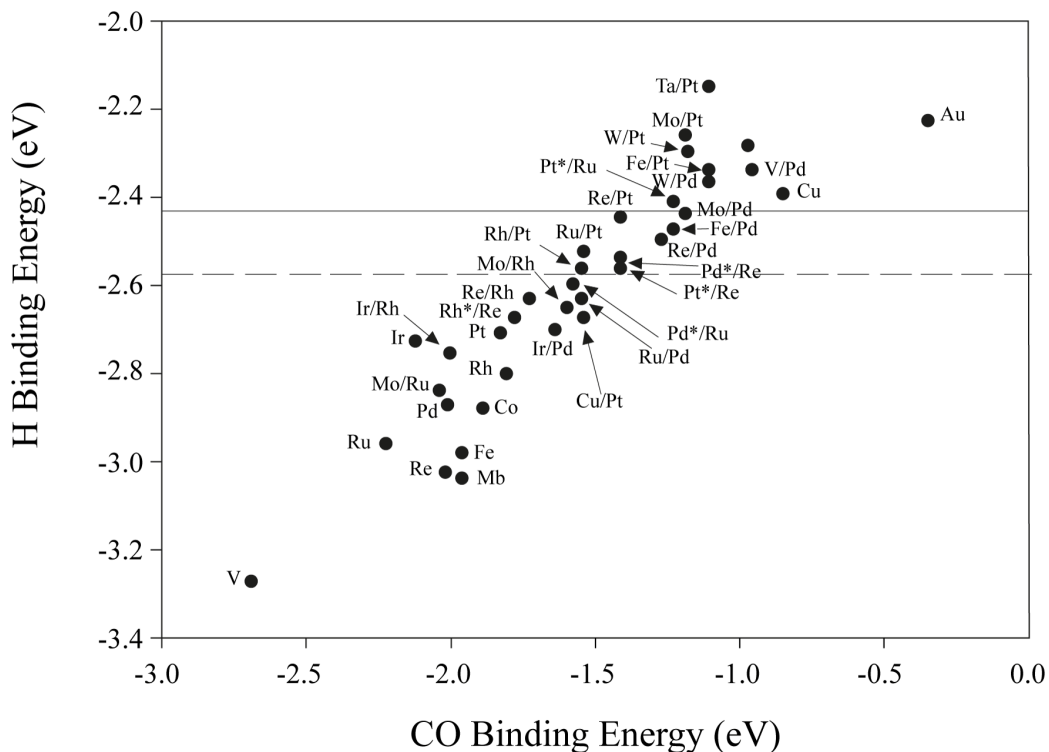


Figure 7. The H binding energy (eV) and CO binding energy (eV) of various transition metal nanoalloys [28].

Puig-Molina et al. reduced and re-oxidized Cu-Pt nanoalloys. XANES was used to observe the change in structure. These researchers found that upon reduction the XANES showed the CuPt cluster was not metallic Cu, Cu/Pt nor Cu_3Pt . They concluded it probably formed another alloy. It was also shown that upon re-oxidation the Cu/Pt structure was different from the fresh sample [37].

The CuPt phase diagram shows ordered phases: CuPt, Cu_3Pt , CuPt_3 and a 1D-LPS [38] (see figure 8). The preferred structures and types are given in Table 2. Figure 8 also shows the amount of mixing between the Cu and Pt atoms. CuPt has 50% Pt as is expected and becomes a liquid at around 1085 K. Cu_3Pt has around 15% Pt which is lower than expected and becomes a liquid around 1005 K. 1D-LPS around 30% Pt and becomes a liquid at around 691 K.

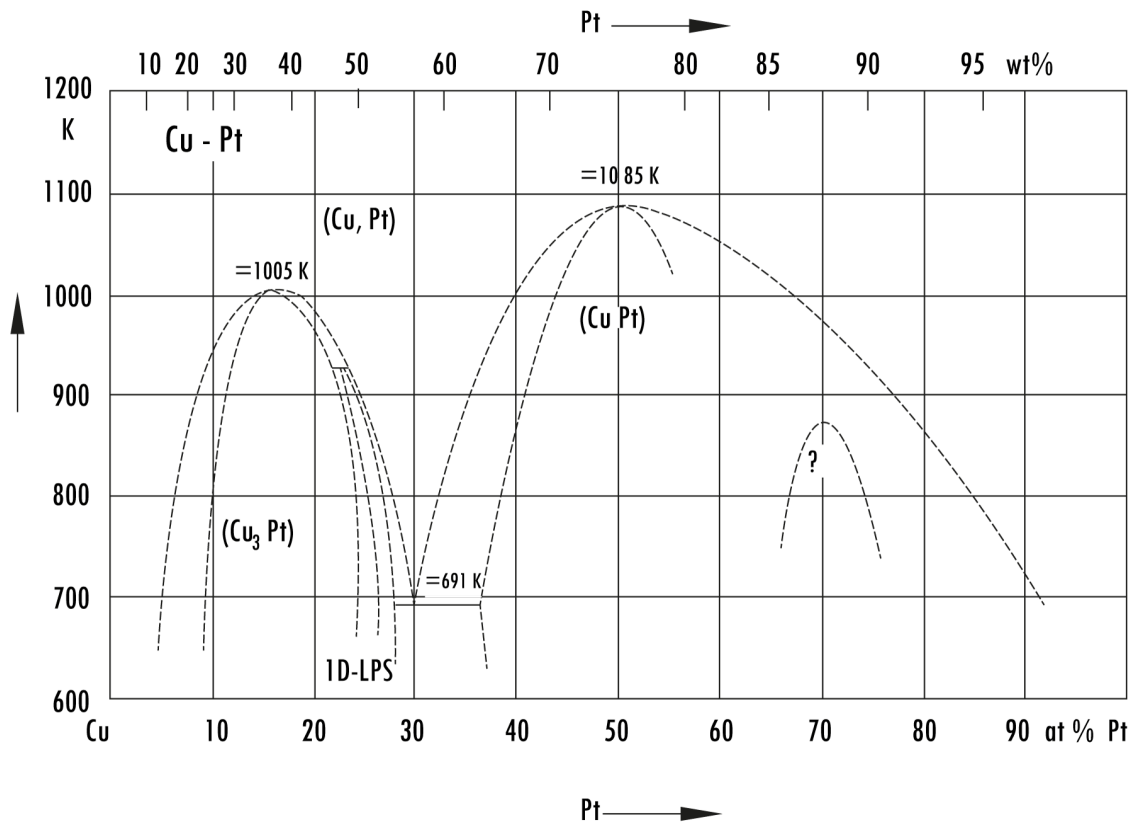


Figure 8. The bulk phase diagram of CuPt [38].

Table 2. CuPt crystal structures and lattice parameters [38].

Phase	Structure	Type	a[nm]	c[nm]
Cu₃Pt	cub	Cu ₃ Au	0.3682	
1D-LPS	tetr	Cu ₃ Pd	0.3715	0.3699
CuPt	Hex	CuPt	1.0713	1.3192
CuPt₃	cub		0.38492	

2.5 Genetic algorithms and the optimization of cluster geometries

Genetic algorithms (GA) were proposed by John Holland in the 70s. They have been used in diverse areas such as chemistry, physics, economy and computer science. These algorithms were inspired in the biologic process of evolution [82].

The search for the lowest potential energy configuration of an atomic nanocluster is a global optimization problem. One of the key aspects of the study of cluster potential energy surfaces (PES), is the number of local minima—that is, of stable configurations—that lie on the PES. This number increases exponentially with the cluster size. The number of local minima on the PES of a Lennard-Jones (LJ) cluster with size $N = 100$, according to the last estimates [84], should be larger than 10 [40].

The global optimization of clusters consists in finding, size and chemical composition being fixed, the structural and chemical arrangement of the lowest lying minimum on the PES [41-46]. To our purposes we may refer to clusters as individuals represented by its atomic coordinates which in biological terms would be its chromosomes [82]. With these elements we produce an initial population that will iterate throughout the following steps:

Selection. It is how the individuals are selected for crossover. Random selection methods can be used such as the roulette wheel which assigns a probability of being selected proportionally to the individual fitness.

Mating. Defines how the parent's chromosomes are combined to produce offspring. Figure 9 shows two examples of commonly techniques for mating.

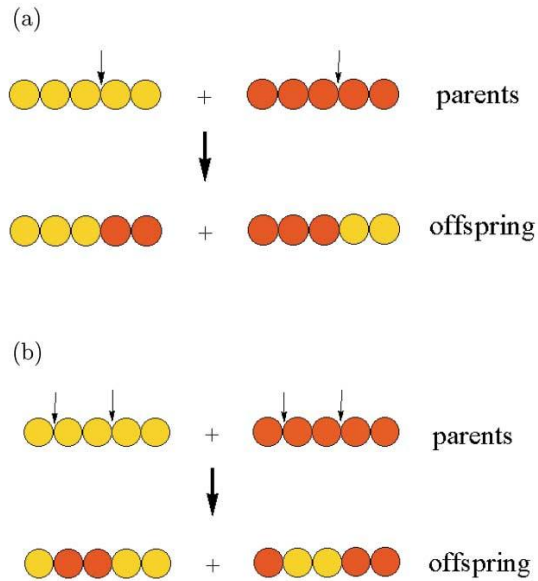


Figure 9. Schematic representation of the crossover operation in a generic GA. (a) One-point crossover—two parents are cut at the same point and offspring are formed by combining complementary genes from parents. (b) Two-point crossover—two parents are cut at the same two points [47].

Mutation. Mating does not introduce new genetic material into the population. This can lead to an optimization that always converges to the same non-optimal solution. Mutation consists on making a few random changes in selected genes of a randomly chosen individual [48].

Natural selection. These two variation generating processes do not always yield individuals which are better adapted according to the fitness criteria and therefore a selection mechanism is also needed to pick up better solutions from a pool of new born individuals [83].

2.6. DFT

Density functional theory is an extremely successful approach for the description of ground state properties of metals, semiconductors, and insulators. The main idea of DFT is to describe an interacting system of fermions via its electronic density and not via its many-body wave function. For N electrons in a solid, which obey the Pauli principle and repulse each other via the Coulomb potential, this means that the basic variable of the system depends only on three -the spatial coordinates x , y , and z - rather than $3*N$ degrees of freedom.

Despite recent improvements, there are still difficulties in using density functional theory to properly describe intermolecular interactions, especially van der Waals forces; charge transfer excitations; transition states, global potential energy surfaces and some other strongly correlated systems; and in calculations of the band gap in semiconductors. Its incomplete treatment of dispersion can adversely affect the accuracy of DFT in the treatment of systems which are dominated by dispersion [53] or where dispersion competes significantly with other effects [54]. The development of new DFT methods designed to overcome this problem, by alterations to the functional [55] or by the inclusion of additive terms [56,57,58] is an important research topic.

This technique is based on the Hohenberg and Kohn theorem [59,60], which states that the energy for a given type of Hamiltonian operator may be described by a unique functional of the density. Since the electronic energy is a unique functional of the electronic density $\rho(r)$, the electronic energy $E_e[\rho]$ of a system of interacting ions and electrons may be expressed as a unique functional $F[\rho]$:

$$E_e[\rho] = F[\rho] + \int \rho(r)v_{\text{ext}}(r) dr + E_{\text{ion}}(\{R_I\}),$$

where $v_{\text{ext}}(r)$ is an external potential of the electron gas, $E_{\text{ion}}(\{R_I\})$ is the ion– ion interaction energy of the ions at fixed positions R_I , and $F[\rho]$ is the universal functional of ρ independent of $v_{\text{ext}}(r)$. Thus $F[\rho]$ is the same functional for electrons in atoms, molecules, polymers or solids. Unfortunately, the exact form of this functional $F[\rho]$ is unknown. However, reasonable approximations to it are now available such as the LDA, the GGA and, so called, hybrid methods [59].

In general, DFT is the most cost effective method for achieving a high degree of accuracy at the quantum-mechanical level. The reliability of DFT results (when calculating properties) depends sensitively on how well the property is described by the electron density, or how the property relates to the electron density.

One way of reducing the computational complexity of DFT, and making large systems (or heavy elements) or longer simulations more practical, is to use a combination of basis sets and inner-core pseudopotentials [61].

The foundations of modern DFT were published in the classic papers of Hohenberg and Kohn in 1964, and Kohn and Sham one year later [60,62]. They developed an exact variational principle formalism in which ground state properties, such as: total electronic energy, equilibrium positions and magnetic moments are expressed in terms of the total electronic density. The two fundamental theorems state that:

Hohenberg and Kohn Theorem: The ground state density of a bound system of interacting electrons in some external potential determines this potential uniquely, as well as the ground state wave function. Also since electronic density determines both, the total number of electrons, N and the external potential; it also provides a full description of all the ground-state observables, which are functional of the electron density [63].

The second statement of the Hohenberg-Kohn theorems states: the ground state energy and the ground-state density of a system characterized by an external potential, can be obtained by using the variational principle. In other words, the ground state energy can be expressed as a functional of the ground state density [59].

So, this theory established the existence of a universal functional, which is independent of the external potential i.e. which has the same functional form for any system considered. From the Hohenberg-Kohn theorems are derived the Kohn-Sham equations [64]. These equations solve the problem of the complex many electron Schrödinger equations, by transforming them into a set of N single-electron equations, which need to be solved self-consistently.

$$\left[-\frac{1}{2}\nabla^2 + V(\vec{r}) + \int \frac{\rho(\vec{r}')}{|\vec{r} - \vec{r}'|} d^3\vec{r}' + V_{xc}[n(\vec{r})] \right] \varphi_i(\vec{r}) = \epsilon_i \varphi_i(\vec{r})$$

with an electronic density:

$$\rho(\vec{r}) = \sum_{i=1}^N |\varphi_i(\vec{r})|^2$$

3. COMPUTATIONAL METHODOLOGY

3.1 The Gupta Potential

The Gupta potential was originally designed to deal with inconsistencies between experimental data and computer simulation [65]. Now is used to model inter-atomic interactions in metal systems [66]. It is a semi-empirical many body potential derived within the tight-binding second-moment approximation. Many-body potentials advantage additive potentials in reproducing some basic properties for metallic systems.

The configurational energy of a cluster is written as the sum over all the atoms of attractive and repulsive energy components:

$$V_{clus} = \sum_i^N \{V^r(i) - V^m(i)\}$$

where the Born-Mayer pair repulsive term $V^r(i)$ is expressed as:

$$V^r(i) = \sum_{j \neq i}^N A(\alpha, \beta) e^{-p(\alpha, \beta) \left(\frac{r_{ij}}{r_0(\alpha, \beta)} - 1 \right)}$$

and the many-body attractive term $V^m(i)$ is expressed as:

$$V^m(i) = \sqrt{\sum_{j \neq i}^N \xi^2(\alpha, \beta) e^{-2q(\alpha, \beta) \left(\frac{r_{ij}}{r_0(\alpha, \beta)} - 1 \right)}}$$

α and β represent the atomic species of atoms i and j , respectively. A , ξ , p and q are the potential parameters that are usually fitted to experimental properties of bulk metals and alloys, such as the cohesive energy, lattice parameters, and independent elastic constants for the reference crystal structure at 0 K. r_0 denotes the nearest neighbor distance of the pure bulk elements, often taken as the average of the pure distances, but it can also be taken as the experimental nearest-neighbor distance in some specific ordered bulk alloy. r_{ij} is the distance between atoms i and j [65].

Values of the Gupta potential parameters describing Pt-Pt and Cu-Cu interactions are taken from the work of Cleri and Rosato [66]. These values are listed in the table below.

Table 3. Gupta potential parameters [65].

parameter	Cu-Cu	Pt-Pt
A	0.0855	0.2975
ξ	1.224	2.695
p	10.960	10.612
q	2.278	4.004
r_0	2.556	2.775

3.1.1 Parameterization of the Gupta Potential

A previous study on nanoalloys concluded that parameters obtained by averaging the parameters of pure elements, gave a good qualitative fit to previous experimental and theoretical studies of bimetallic clusters [67]. In this study, the heteronuclear Cu-Pt Gupta potential parameter set $\{P\}$ is derived as the weighted average of the corresponding pure metal Cu-Cu and Pt-Pt parameters:

$$P(\text{Cu-Pt}) = w_1P(\text{Cu-Cu}) + w_2P(\text{Pt-Pt})$$

Weighting parameters have been investigated in the range $0 \leq w \leq 1$, in steps $\Delta w = 0.1$. This is called symmetrical weighting of all parameters, since all of the parameters vary in the same way. That is, from the value for Pt-Pt ($w = 0$) to the value for Cu-Cu ($w = 1$) [52]. Therefore, the Gupta potential parameters $\{P\} = \{A, \xi, p, q \text{ and } r_0\}$ are obtained as:

$$P(\text{Cu-Pt}) = wP(\text{Cu-Cu}) + (1 - w)P(\text{Pt-Pt})$$

Table 4. Parameter set values.

w	0.0	0.1	0.2	0.3	0.4	0.5	0.6	0.7	0.8	0.9	1.0
A	0.2975	0.2763	0.2551	0.2339	0.2127	0.1915	0.1703	0.1491	0.1279	0.1067	0.0855
ζ	2.695	2.548	2.401	2.254	2.107	1.960	1.812	1.665	1.518	1.371	1.224
p	10.612	10.647	10.682	10.716	10.751	10.786	10.821	10.856	10.890	10.925	10.960
q	4.004	3.831	3.659	3.486	3.314	3.141	2.968	2.796	2.623	2.451	2.278
r_0	2.775	2.753	2.731	2.709	2.687	2.666	2.644	2.622	2.600	2.578	2.556

3.2 The Birmingham Cluster Genetic Algorithm

The Birmingham Cluster Genetic Algorithm (BCGA) is a program that has been used to find the putative local minima as well as other low-lying energy structures [78]. The operation of this GA optimization program is shown in figure 10.

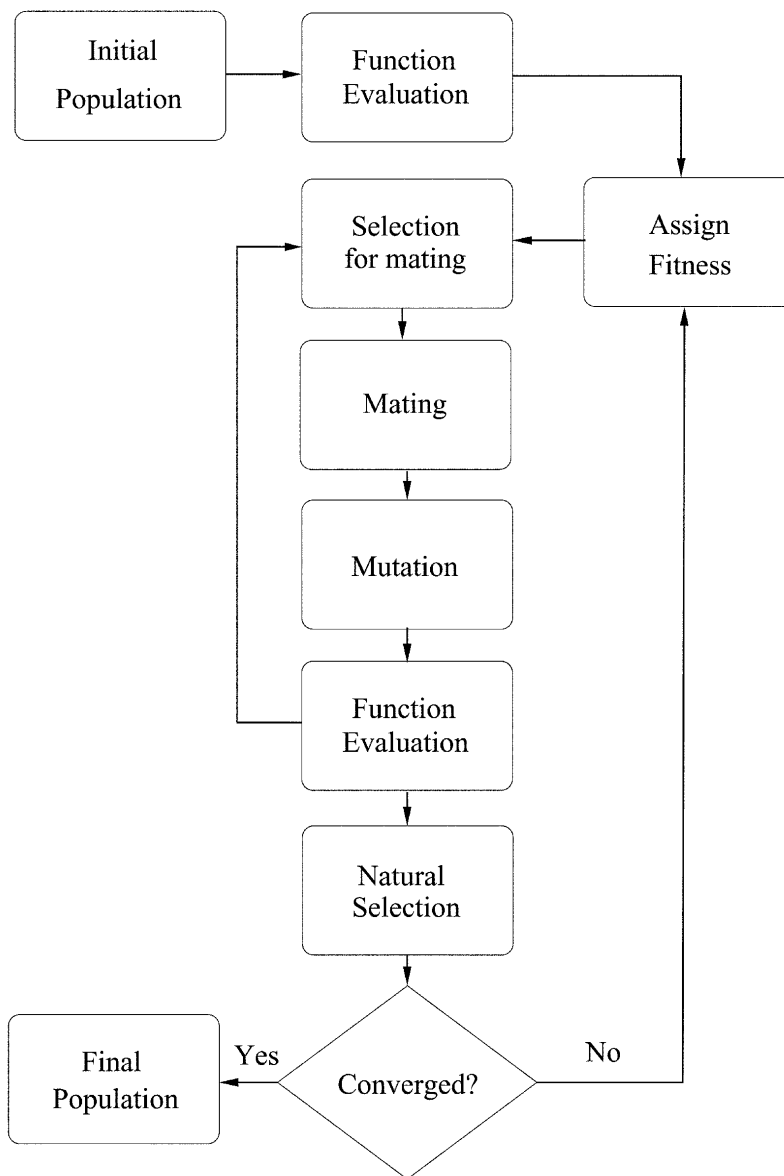


Figure 10. Flow chart for the BCGA program [47,48].

For a given cluster size (N), a number of clusters, (N_{pop} , typically from 10 to 30) are generated at random to form the initial population. The x , y and z coordinates are real values on the Cartesian space [49]. These values are chosen randomly in the range $[0, N^{1/3}]$ [47]. This ensures that the cluster volume scales correctly with cluster size (i.e. linearly with N). All of the clusters in the initial population are then relaxed into the nearest local minima, by minimizing the cluster potential energy as a function of the cluster coordinates, using the quasi-Newton L-BFGS routine [50,51].

As the cluster GA is being used to minimize the cluster potential energy (V_{clus}), the lowest energy clusters have the highest fitness and the highest energy clusters have the lowest fitness.

Dynamic scaling is achieved by using a normalized value of the energy, ρ , in the fitness calculations:

$$\rho_i = (V_i - V_{min}) / (V_{max} - V_{min})$$

where V_{min} and V_{max} are the lowest and highest energy clusters in the current population, respectively. The most common fitness functions that have been used are:

Exponential:

$$f_i = e^{-\alpha\rho_i}$$

where α is typically set to 3.

Linear:

$$f_i = 1 - 0.7\rho_i$$

Hyperbolic tangent:

$$f_i = \frac{1}{2} [1 - \tanh(2\rho_i - 1)]$$

The choice of fitness function controls how rapidly fitness falls off with increasing cluster energy.

The selection of parents is accomplished using either roulette wheel or tournament selection. In both of these selection schemes, low energy clusters are more likely to be selected for crossover and therefore to pass their structural characteristics on to the next generation. Once a pair of parents has been selected, they are subjected to the crossover operation.

Crossover in this implementation consists of random rotations that are performed on both parent clusters and then both clusters are cut horizontally about one or two positions parallel to the xy plane, and complementary fragments are spliced together. For the single cut method, the cutting plane can be chosen at random; it can be defined to pass through the middle of the cluster, or weighted according to the relative fitness of the two parents. For the double cut method, the cutting planes are chosen at random.

Crossover continues until a predetermined number of offspring (N_{off}) have been generated. The number of offspring is generally set to approximately 80% of the population size. Each offspring cluster is subsequently relaxed into the nearest local minimum, as described above. The local minimization step obviously changes the structure of the offspring cluster, and this structural rearrangement will be greatest in the region of the join between the two fragments donated by its parents. As the clusters get larger, however, the perturbation due to the local minimization should become relatively smaller and confined to the join region. In this way, the principle of schemata should apply, as parents with high fitness are more likely to have fit offspring by passing on fragments with low energy arrangements of atoms.

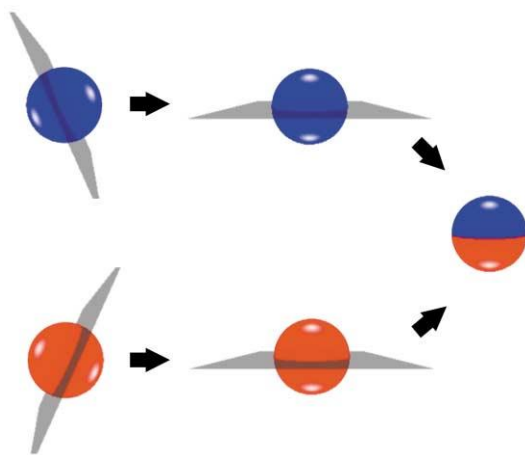


Figure 11. Schematic representation of the Deaven–Ho cut and splice crossover operation, as implemented in our GA program. (Single cut crossover is shown) [47].

In an attempt to avoid stagnation and to maintain population diversity, a mutation operator is introduced, whereby each individual has a probability (P_{mut}) of undergoing mutation. The mutation perturbs some or all of the atoms within the cluster.

Some of the mutation schemes that can be adopted include: atomic displacement, twisting, cluster replacement, atom permutation. After mutation, each “mutant” cluster is subsequently relaxed into the nearest local minimum, using the L-BFGS minimization routine.

The new population is selected from the N_{pop} lowest energy clusters selected from the set containing the old population, the new offspring clusters and the mutated clusters. The inclusion of clusters from the previous generation makes the GA elitist, ensuring that the best member of the population cannot get worse from one generation to the next.

Once the new generation has been formed, the potential energies of the best (V_{min}) and worst (V_{max}) members of the population are recorded and the fitness values calculated for the entire population. The whole process of crossover, mutation and selection is then repeated for a specified number (N_{gen}) of generations or until the population is deemed to have converged. The population is considered to be convergent if the range of cluster energies in the population has not changed for a prescribed number of generations [47].

A considerable amount of effort has been expended in optimizing the GA operations and parameters described above [52]. Because of the stochastic nature of the GA, the GA program is run several times for each cluster’s nuclearity and for each set of operations/parameters. It is generally found that there is not a great dependence of the success rate of finding the global minimum structure on the type of fitness function used, though even small improvements are useful, especially for larger cluster sizes. For larger clusters, a larger population size and maximum number of generations is generally required [47].

In our instance we use the convergence criterion limited to a maximum of 400 generations and a population of 40 clusters. For a given cluster size, 38 in our case, coordinates of the atoms are randomly generated and normalized.

3.3 Energetic Analysis

When studying fixed-size bimetallic clusters, the excess (or mixing) energy as a function of composition, Δ_N , is a useful quantity. For binary nanoalloys with fixed size ($N = 38$ atoms) but different compositions, Δ_N is defined as:

$$\Delta_N = E_N(A_M B_{N-M}) - M \frac{E_N(A_N)}{N} - (N - M) \frac{E_N(B_N)}{N}$$

where $E_N(A_M B_{N-M})$ is the total energy of a given cluster calculated at the Gupta level and $E_N(A_N)$ and $E_N(B_N)$ are the total energies of the global minima of the pure metal clusters (i.e. Cu_N and Pt_N) [52]. This excess energy is an unbiased quantity, defined as zero for the global minima of the pure clusters. Negative values of Δ_N indicate that mixing is favorable.

3.4 Chemical Ordering

Binary nanoalloys generally present more complex structures than monometallic clusters and global optimization is more difficult due to the existence of homotops [6], which are isomers with the same geometry and composition but with a different arrangement of the two types of atoms. For an A-B alloy system, the chemical order parameter, σ is defined as:

$$\sigma = \frac{N_{A-A} + N_{B-B} - N_{A-B}}{N_{A-A} + N_{B-B} + N_{A-B}}$$

where N_{A-B} is the number of nearest-neighbor A-B bonds and N_{A-A} and N_{B-B} denote the numbers of homonuclear bonds in the binary cluster [69]. The σ value is positive when cluster segregation occurs, close to zero when disordered mixing takes place, and negative when there is more ordered mixing including layering and onion-like configurations [16].

3.5 Density Functional Theory

DFT calculations were performed using the NWChem quantum chemistry package [70] and the Perdew-Wang exchange-correlation functional (PW91) [71,72]. The electronic exchange energy as a functional of the density may be approximated as:

$$E_x[n] = A_x \int d^3r n^{4/3} F(s)$$

where:

$$s = \frac{|\nabla n|}{2k_F n}, k_F = (3\pi^2 n)^{1/3}, F(s) = (1 + 1.296s^2 + 14s^4 + 0.2s^6)^{1/15}$$

Unlike most other functionals this one is simple enough to be applied routinely in self-consistent calculations for atoms, molecules and solids. On the other side is important to note that the self-consistent valence electron density in an atom is still somewhat too diffuse [71].

Often due to the limited accuracy of semiempirical potentials, DFT reoptimization may significantly change the energetic ordering of clusters belonging to different structural motifs [73]. In order to verify this possibility we chose low energy structures generated by the BCGA and performed reoptimization calculations.

3.6 Pair Distribution Function

The PDF gives the probability of finding two atoms separated by a distance r [74]. This function is obtained by integrating the distribution functions over the positions of all atoms excluding the two atoms measured. We must also include appropriate normalization factors. We use a definition that takes into account the averages over the ensemble atom pairs which is useful in computer simulations [75].

$$g_p(\vec{r}) = \frac{V}{N^2} \left\langle \sum_i^N \sum_{j \neq i}^N \delta[\vec{r} - \vec{r}_{ij}] \right\rangle$$

The PDF is important because it allows the characterization of the lattice structure of the nanoalloys [76]. In our study we use it to structurally compare the motifs generated using the BCGA technique and the motifs that have been reoptimized with the DFT method. This allows an objective and quantitative comparison of the structures.

4. RESULTS AND DISCUSSION

4.1 BCGA Structures

One hundred structures were computed varying its weighting and composition. Structures found for a given weighting and composition are not all the same. We chose to keep those with the lowest energy. A diagram with a summary of structural variety across compositions and weightings is shown below (Figure 12).

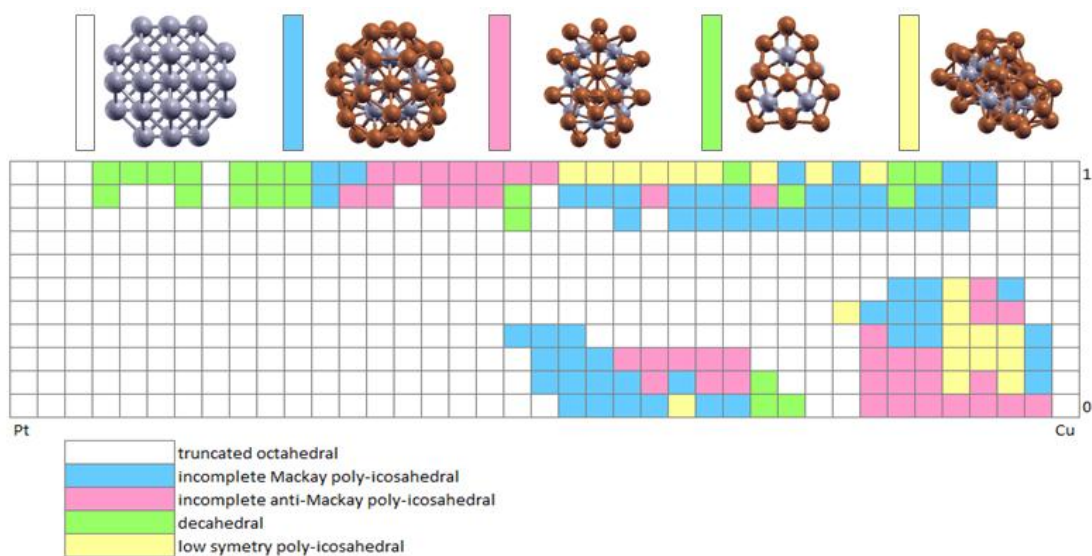


Figure 12. Structure map for all weightings and compositions.

Structures for a given weighting vary with composition in most cases. For $w = 0.0$ the predominant structure is the TO (Figure 13a). But as the copper atoms proportion increases on the mix we can find other lower symmetry motifs. Those include the iMpIh (Figure 13b), the iaMpIh and a few Dh symmetries. Except for the pure copper cluster which also has the TO structure.

For $w = 0.6$ and $w = 0.7$ we found exclusively TO structures for all compositions. For $w = 1.0$ and $w = 0.9$ a wide variety of the mentioned structures was found. Also these weightings showed a higher degree of segregation (Figure 13c).

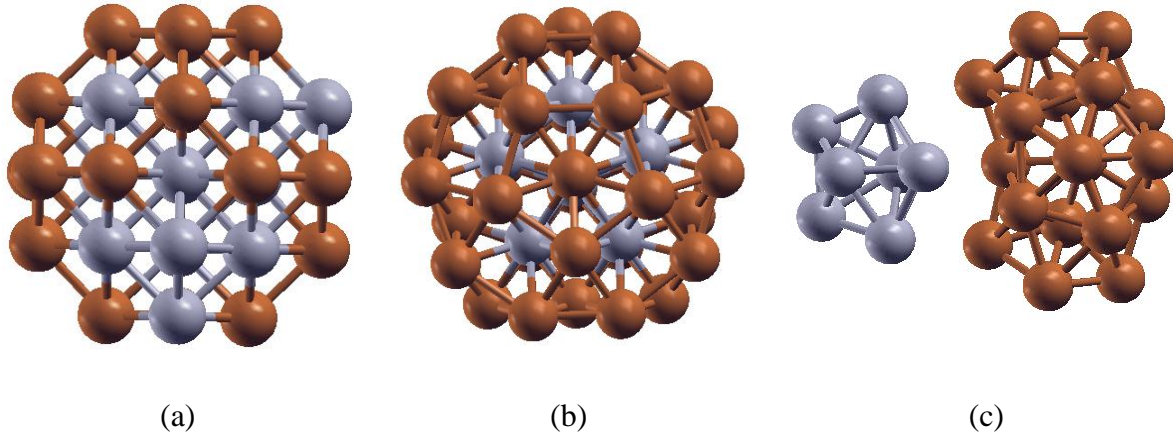


Figure 13. Three remarkable structures. (a) The TO was the most abundant structure found by the BCGA. (b) The iMpIh was also a common structure especially when copper concentrations are high. (c) A highly segregated (Janus-type) composition (note that this motif is not included in our results because it was not the one with the lowest energy).

4.2 Excess Energy

We calculated the excess energy for all weightings as a function of composition (Figure 14). It is clear the increase of excess energy as the weighting goes from $w = 0.0$ to $w = 1.0$. For compositions with weighting factor of 0.7 and below, the excess energy is negative. A more negative excess energy indicates that mixing is favorable.

The lowest values for every composition are those of weighing factor $w = 0.0$. The lowest value is -44.0 eV and belongs to the composition $\text{Cu}_{26}\text{Pt}_{12}$. For $w = 0.8$ excess energy remains very close to zero. Weightings of 0.9 and 1.0 have all positive, yet small values. The highest value is 3.05 eV for $w = 1.0$ at composition $\text{Cu}_{20}\text{Pt}_{18}$.

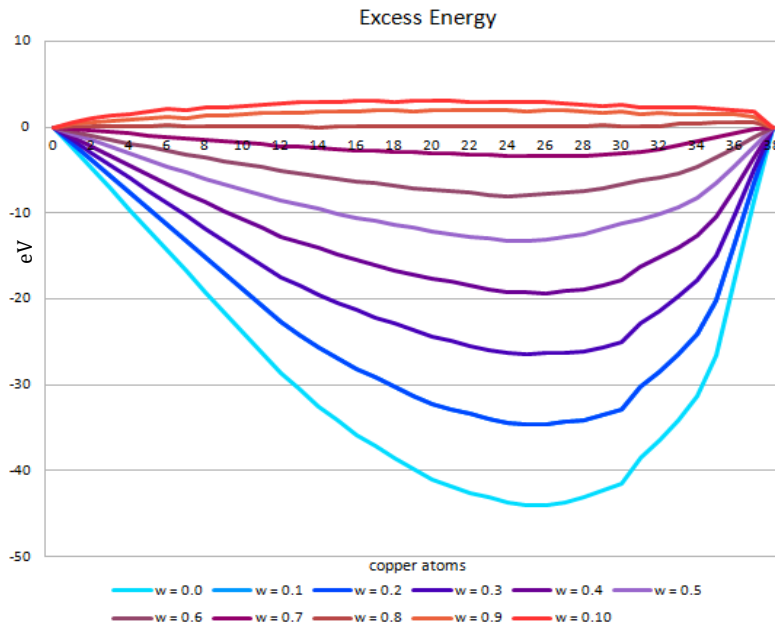


Figure 14. Excess energy for all weightings and compositions.

4.3 TO vs iMpIh, energy comparison.

The energies of TO and iMpIh were particularly close when using a weighting factor of 0.6. We made an energy comparison plot in which we subtract the energy of TO to the energy of iMpIh. That means that for positive values on the plot TO energy is lower than iMpIh and vice versa.

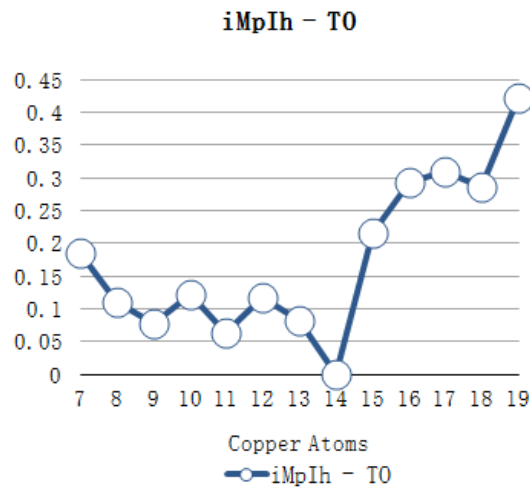


Figure 15. Energy comparison between iMpIh and TO.

As we can observe in the plot the iMplh energy is never lower than the TO energy. But their energies happen to match at composition $\text{Cu}_{14}\text{Pt}_{24}$. However, we kept the TO as the selected structure for this study.

4.4 Chemical Ordering

The chemical ordering of the structures found varies along with weighting and composition. Of these two quantities weighting has the stronger influence. In general for structures with weighting values of 0.0, 0.1, 0.2, 0.3 homogeneous mixing takes place (Figure 16a). Additionally, when there are very few atoms of Pt we found multi-core-shell structures (Figure 16b). We also found some layering profiles for these values of w (Figure 16c).

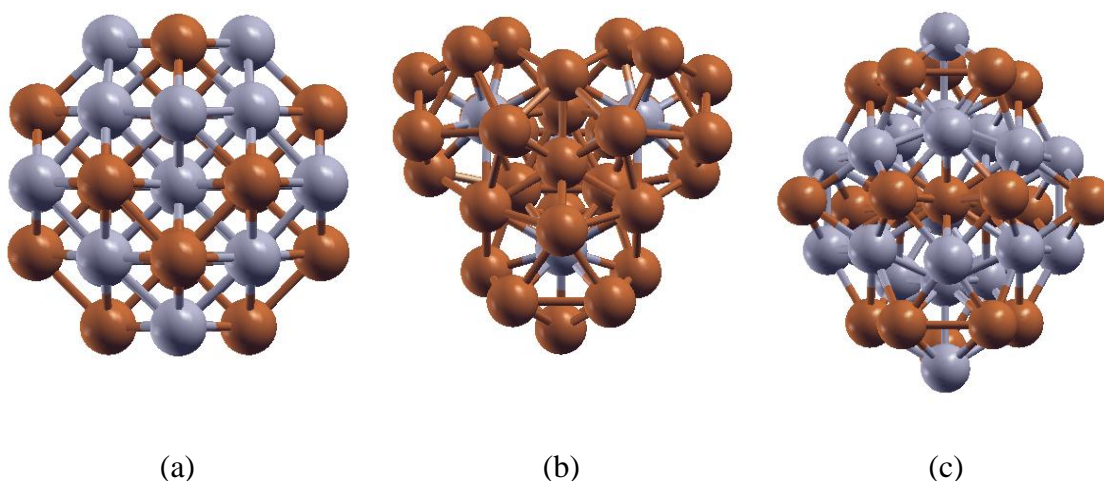


Figure 16. Mixing patterns. (a) Structure $\text{Cu}_{18}\text{Pt}_{20}$ ($w = 0.1$) displaying homogeneous mixing. (b) Structure $\text{Cu}_{34}\text{Pt}_4$ ($w=0.0$) is a multi-core shell structure with 4 cores of Pt. (c) Structure of $\text{Cu}_{19}\text{Pt}_{19}$ ($w = 0.1$) shows a layering profile.

For weighing values ranging 0.4-0.7 copper atoms tend to be on the surface, thus producing simple core-shell ordering when copper atoms cover the entire surface. On the other hand, for weighting values 0.8-1.0 we found a high degree of segregation. The most common chemical ordering profile for these weightings was ball-and-cup. We also calculated the number of different types of bonds per composition for $w=0.5$ (Figure 17) [78].

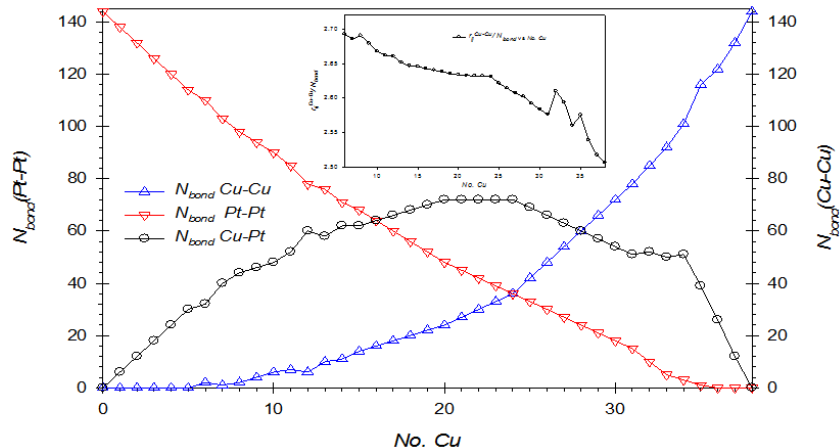


Figure 17. Number of bonds per composition ($w=0.5$).

Using a program to measure the number of bimetallic bonds [77], we can observe in the plot that the number of monometallic bonds is always greater to the bimetallic bonds. Also bimetallic bonding is more frequent when there are more Cu atoms.

4.5 Density Functional Theory and Average Nearest Neighbor Distance

DFT calculations are computationally expensive so we took a few arbitrary structures to work with. Reoptimization with DFT did not dramatically change the structural motif. Instead, there were small, almost imperceptible, changes in the interatomic distances. We made a detailed study of the $\text{Cu}_{32}\text{Pt}_6$ composition for weighting $w = 0.5$. We show the structural motifs before and after optimization (Figure 18).

To take a closer look to these small changes we calculated and plotted the ANND. This plot compares the GA optimization vs. the DFT reoptimization. Using a program to calculate ANND [77] we get the following plot.

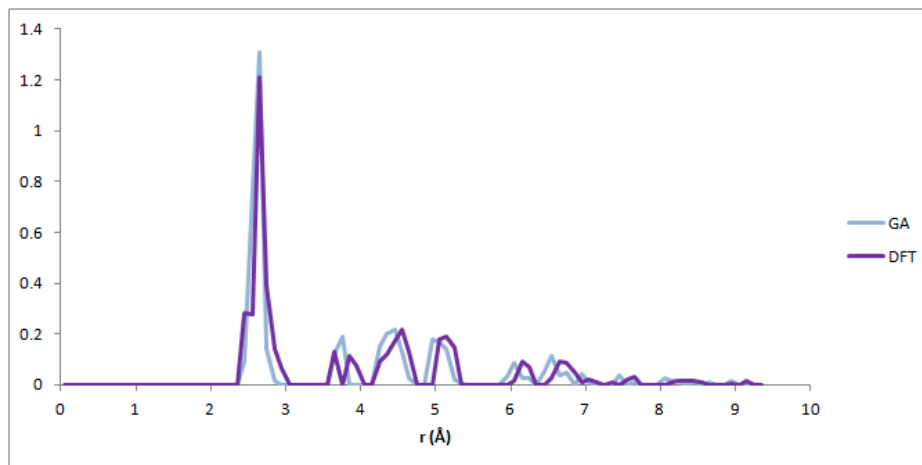


Figure 19. ANND of $\text{Cu}_{32}\text{Pt}_6$ ($w = 0.5$) before (GA optimization) and after DFT reoptimization.

There are a few things to point out on the ANND plot. First the DFT plot is slightly shifted to the right. This confirms the fact that interatomic distances increased. Also the second peak of the GA plot is split in on the DFT plot. This can be due to a small deformation on the structure.

4.6 Scanning transmission electron microscopy

Theoretical results need to provide a point of comparison with experimental data. STEM simulation is a simple and yet effective approach to this goal. We performed STEM simulation for the composition $\text{Cu}_{32}\text{Pt}_6$ as sample structure which is weighted by $w = 0.0$. In the images below is easy to notice that the red spots correspond to the Platinum atoms and the violet ones to Copper.

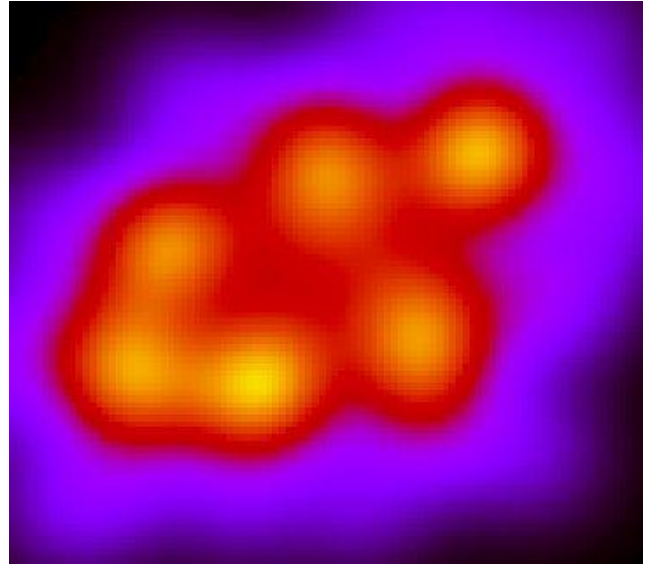
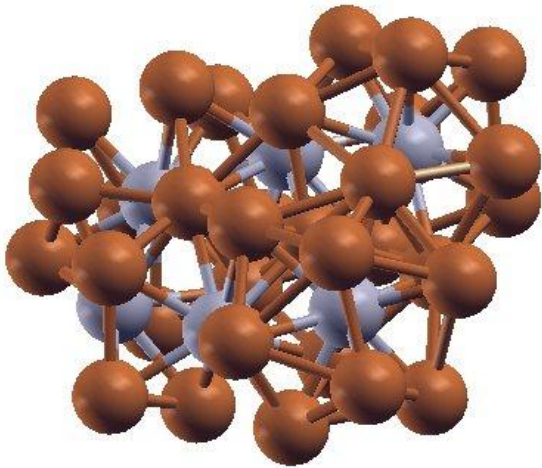


Figure 20. STEM simulation of Cu₃₂Pt₆ ($w = 0$). The high intensity spots (yellow) show the location of the platinum atoms. The violet zone is filled with copper atoms.

Color intensity on the graph is proportional to the atomic column height as well as the atomic number i.e. 29 for Cu and 78 for Pt. Pt atoms are brighter because Pt atomic number is higher than Cu [79]. A more advanced technique described by Li et al. can be used to produce a three-dimensional representation of the structure [80].

5. CONCLUSIONS

Even when there is no experimental fit to compare with, we came across some interesting observations. It is apparent from results that a greater variety of structures occurs when parameters are biased to Cu characteristics ($w \rightarrow 1$) or when composition contains a high number of Cu atoms. Also a higher degree of segregation was found with the mentioned weighting. On the other hand the most stable structures overall are those weighted towards Pt characteristics ($w \rightarrow 0$). Also a higher degree of mixing was noticed with the mentioned weighting. There is a preference for the TO structure when there is abundance of Pt atoms or parameters are weighted towards Pt.

When the weighting parameter is biased towards zero the total excess energy of the composition is lower than parameters that tend to 1. STEM simulation successfully produced images that can be easily compared with experimental results.

REFERENCES

1. Johnston R.L. 2002. *Atomic and molecular clusters*. Taylor and Francis. London and New York. p. 249.
2. Roduner E. 2006. Size matters: why nanomaterials are different. *Chem. Soc. Rev.* 35: 583-592.
3. Roduner E. 2006. *Nanoscope materials: Size-dependent phenomena*. The Royal Society of Chemistry. Cambridge. p. 285.
4. Feynman, R. 1960. *There's Plenty of Room at the Bottom*, originally published in the February 1960 issue of Caltech's Engineering and Science Magazine.
5. Baletto F., and Ferrando R. 2005. Structural properties of nanoclusters: energetic, thermodynamic, and kinetic effects. *Rev. Mod. Phys.* 77: 371-423.
6. Ferrando R., Johnston R. L., and Jellinek. 2008. Nanoalloys: from theory to applications of alloy clusters and nanoparticles. *J. Chem. Rev.* 108: 845-910.
7. Jain P.K., El-Sayed I.H., and El-Sayed M.A. 2007. Au nanoparticles target cancer. *Nanotoday*. 2: 18-29.
8. Jellinek J. 1999. *Theory of atomic and molecular clusters*. Springer. Berlin. p. 433.
9. Krissinel E.B., and Jellinek J. 1997. 13-atom Ni-Al alloy clusters: structures and dynamics. *Int. J. Quantum Chem.* 62: 185-197.
10. Darby S., Mortimer-Jones T.V., Johnston R.L., and Roberts C. 2002. Theoretical study of Cu-Au nanoalloy clusters using a genetic algorithm. *J. Chem. Phys.* 116: 1536-1550.

11. Massen C., Mortimer-Jones T.V., and Johnston R.L. 2002. Geometries and segregation properties of platinum-palladium nanoalloy clusters. *J. Chem. Soc. Dalton Trans.* 23: 4375-4388.
12. Lloyd L.D., Johnston R.L., Salhi S., and Wilson N.T. 2004. *J. Mater. Chem.* 14: 1691-1704.
13. Lloyd L.D., Johnston R.L., Salhi S. 2005. Strategies for increasing the efficiency of a genetic algorithm for the structural optimization of nanoalloy clusters. *J. Comp. Chem.* 26: 1069-1078.
14. Paz-Borbón L.O., Johnston R.L., Barcaro G., and Fortunelli A. 2007. A mixed structural motif in 34-atom Pd-Pt clusters. *J. Phys. Chem. C.* 111: 2936-2941.
15. Paz-Borbón L.O., Johnston R.L., Barcaro G., and Fortunelli A. 2008. *J. Chem. Phys.* 128: 134517-134528.
16. Paz-Borbón L.O., Gupta A., and Johnston R.L. 2008. Dependence on the structure and chemical ordering of Pd-Pt nanoalloys on potential parameters. *J. Mater. Chem.* 18: 4154-4164.
17. Pittaway F., Paz-Borbón L.O., Johnston R.L., Arslan H., Ferrando R., Mottet C., Barcaro G., and Fortunelli A. 2009. Theoretical studies of palladium-gold nanoclusters: Pd-Au clusters with up to 50 atoms. *J. Phys. Chem. C.* 113: 9141-9152.
18. Fielicke, A. 2008. *Reactivity and Catalysis* <http://www.fhi-berlin.mpg.de/mp/fielicke/>
19. Fielicke, A. 2008. A personal communication.
20. Bazin D., Guillaume D., Pichon Ch., Uzio D., Lopez S. 2005. *Oil Gas. Sci. Tech. Rev. IFP.* 60: 801.

21. Sao-Joao S., Giorgio S., Penisson J. M., Chapon C., Bourgeois S., and Henry C. 2005. *J. Phys. Chem. B.* 109: 342.
22. Ferrer D., Blom D., Allard L.F., Mejia-Rosales S. J., Pérez-Tijerina E., and José-Yacamán M. 2008. *J. Mater. Chem.* 18: 2442.
23. Paz-Borbón L.O. 2011. *Computational studies of transition metal nanoalloys.* Springer. Berlin. p. 180.
24. Kirkland E.J. 2006. *Image simulation in transmission electron microscopy.* Kavli summer school.
25. Kirkland E.J. 1998. *Advanced computing in electron microscopy.* Plenum. New York. p. 250.
26. Gajdos M. and Hafner J. 2005. CO adsorption on Cu(111) and Cu(001) surfaces: improving site preference in DFT calculations. *Surface Science.* 590: 117–126.
27. Zeinalipour-Yazdi C.D., Cooksy A.L., and Efstathiou A.M. 2008. CO adsorption on transition metal clusters: Trends from density functional theory. *Surface Science.* 602: 1858-1862.
28. Liu P. Logadottir A., and Nørskov J.K. 2003. Modelling the electro-oxidation of CO and H₂/CO on Pt, Ru, PtRu and Pt₃Sn. *Electrochimica Acta.* 48: 3731-3742.
29. Watkins J. 2010. *Investigation of bimetallic CuPt nanoclusters.* School of chemistry. University of Birmingham.
30. Hajghassem H., Banihashemian S.M., and Aliahmadi M. 2009. Low magnetic field detection using a CuPt nanostructure made on a SiO₂/Si structure. *Sensors.* 9: 9734-9740.

31. Zhou S., Varughese B., Eichhorn B., Jackson G., and Kevin McIlwrath. 2005. Pt–Cu Core–Shell and Alloy Nanoparticles for Heterogeneous NO_xReduction: Anomalous Stability and Reactivity of a Core–Shell Nanostructure. *Angewandte Chemie*. 117: 4615-4619.
32. Carino E.V., and Crooks R.M. 2011. Characterization of Pt-Cu core-shell dendrimer-encapsulated nanoparticles synthesized by Cu underpotential deposition. *Langmuir*. 27: 4227-4235.
33. Chen X., Chu W, Cai Q., Xia D., Wua Z., and Wuae Z. 2006. Electronic structure of nanoscale of Cu/Pt alloys: a combined X-ray diffraction and X-ray absorption investigation. *Radiation Physics and Chemistry*. 75: 1622–1625
34. Abdelsayed V., Aljarash A., El-Shall M.S., Othman Z.A.A., and Alghamdi A.H. 2009. Microwave Synthesis of Bimetallic Nanoalloys and CO Oxidation on Ceria-Supported Nanoalloys. *Chem. Mater*. 21: 2825-2834.
35. Avdeev V.I., Kovalchuk V.I., Zhidomirov G.M., DaItri J.L. 2005. Ethylene adsorption on the Pt–Cu bimetallic catalysts. Density functional theory cluster study. *Surface science*. 583: 46–59.
36. Greeley J., and Mavrikakis M. 2006. Neat surface alloys for hydrogen fuel cell applications. *Catalysis Today*. 111: 52–58.
37. Puig-Molina A., Janssens T.V.W., Boisen A., Kooyman P., and Molenbroek A.M. In situ XAFS study of alloy formation in supported CuPt nanoparticles. Delf University of

Technology. http://hasyweb.desy.de/science/annual_reports/2006_report/part1/contrib/41/16778.pdf.

38. Adachi K., D. Bonnenberg, Franse J.J.M., Gersdorf R., et al. 1986. Elements, alloys and compounds. Springer verlag, Berlin. Vol. 19.
39. Ercoç S. 1997. Empirical many body potential energy functions used in computer simulations of condensed matter properties. *Phys. Rep.* 278: 79-105.
40. Doye J.P.K. in *Global Optimization Selected Case Studies*, ed. J. D. Pintér, Kluwer, Dordrecht, in press.
41. Wales D.J. 2003. *Energy Landscapes with Applications to Clusters, Biomolecules and Glasses*; Cambridge University Press: Cambridge, U.K.
42. Doye J.P.K., and Dales D.J. 1997. Structural consequences of the range of the interatomic potential: A menagerie of clusters. *J. Chem. Soc., Faraday Trans.* 93: 4223-4231.
43. Holland J.H. 1992. *Adaptation in Natural and Artificial Systems*. University of Michigan Press. p. 211.
44. Goldberg D.E. 1989. *Genetic Algorithms in Search, Optimization and Machine Learning*. Addison-Wesley. Reading, MA. p. 412.
45. Mitchell M. 1998. *An Introduction to Genetic Algorithms*. MIT Press. Cambridge, MA. p. 209.
46. Cartwright H.M. 2004. *Applications of Evolutionary Computing in Chemistry*. Ed. R. L. Johnston. *Struct. Bonding*. Berlin. p. 184.
47. Johnston R.L. 2003. Evolving better nanoparticles: genetic algorithms for optimizing

- cluster geometries. *Dalton Trans.* 32: 4193-4207.
48. Johnston R.L., and Roberts C. 1999. *Cluster Geometry Optimization Genetic Algorithm Program*, University of Birmingham. Birmingham, U.K.
49. Zeiri Y. 1995. Prediction of the lowest energy structure of clusters using a genetic algorithm. *Phys. Rev. E.* 51: 2769-2772.
50. Byrd R.H., Lu P., Nocedal J., and Zhu C. 1995. A limited memory algorithm for bound constrained optimization. *SIAM J. Sci. Comput.* 16: 1190-1208.
51. Roberts C. 2001. *Genetic algorithms for cluster optimization*. PhD thesis. University of Birmingham.
52. Isamil R., and Johnston R.L. 2010. Investigation of the structures and chemical ordering of small Pd-Au clusters as a function of composition and potential parameterization. *Phys. Chem. Chem. Phys.* 12: 8607-8619.
53. Van Mourik T., and Gdanitz R. J. 2002. A critical note on density functional theory studies on rare-gas dimers. *Journal of Chemical Physics.* 116: 9620–9623.
54. Vondrášek J., Bendová L., Klusák V., and Hobza P. 2005. Unexpectedly strong energy stabilization inside the hydrophobic core of small protein rubredoxin mediated by aromatic residues: correlated ab initio quantum chemical calculations. *J. Am. Chem. Soc.* 127: 2615–2619.
55. Grimme S. 2006. Semiempirical hybrid density functional with perturbative second-order correlation. *J. Chem. Phys.* 124: 034108.
56. Zimmerli U., Parrinello M., and Koumoutsakos P. 2004. Dispersion corrections to density functionals for water aromatic interactions. *J. Chem. Phys.* 120: 2693–2699.

57. Grimme S. 2004. Accurate description of van der Waals complexes by density functional theory including empirical corrections. *J. Comput. Chem.* 25: 1463–1473.
58. Von Lilienfeld O. A., Tavernelli I., Rothlisberger U., and Sebastiani D. 2004. Optimization of effective atom centered potentials for London dispersion forces in density functional theory. *Phys. Rev. Lett.* 93: 153004.
59. Parr R.G., and Yang W. 1989. *Density-Functional Theory of Atoms and Molecules*. Oxford: Scientific Publications. United States. p. 333.
60. Hohenberg P., and Kohn W. 1964. Inhomogeneous electron gas. *Phys. Rev.* 136: B864–B8671.
61. Barnard A.S. 2010. Modeling of nanoparticles: approaches to morphology and evolution. *Rep. Prog. Phys.* 73: 086502.
62. Kohn W., and Sham L.J. 1965. Self-consistent equations including exchange and correlation effects. *Phys. Rev.* 140: A1133-A1138.
63. Kohn W. 1999. Nobel lecture: electronic structure of matter-wave functions and density functionals. *Rev. Mod. Phys.* 71: 1253-1266.
64. Cramer C.J. 2002. *Essentials of computational chemistry*. John Wiley & Sons, LTD. United States. p. 618.
65. R. P. Gupta. 1981. Lattice relaxation at a metal surface. *Phys. Rev. B*, Vol. 23, p. 6265-6270.
66. Cleri F., and Rosato V. 1993. Tight-binding potentials for transition metals and alloys. *Phys. Rev. B.* 48: 22-33.
67. Massen C., Mortimer-Jones T.V., and Johnston R.L. 2002. Geometries and segregation of platinum-paladium nanoalloy clusters. *J. Chem. Soc., Dalton Trans.* 23: 4375-4388.

68. Deaven D.M., and Ho K.M. 1995. Molecular geometry optimization with a genetic algorithm. *Phys. Rev. Lett.* 75: 288-291.
69. Paz-Borbón L.O. Montimer-Jones T.V., Johnston R.L., Posada-Amarillas A., Barcaro G., and Fortunelli A. 2007. Structures and energetics of 98-atom Pd-Pt nanoalloys: potential stability of the Leary tetrahedron for bimetallic nanoparticles. *Phys. Chem. Chem. Phys.* 9: 5202-5208.
70. Kendall R.A., Apr`a E., Bernholdt D.E., Bylaska E.J., Dupuis M., Fann G.I., Harrison R. J., Ju J., Nichols J.A., Nieplocha J., Straatsma T.P., Windus T.L., and Wong A.T. 2000. High performance computational chemistry: an overview of NWChem a distributed parallel application. *Comput. Phys. Commun.* 128: 260-283.
71. Perdew J.P., and Wang Y. 1986. Accurate and simple density functional for the electronic change energy: generalized gradient approximation. *Phys. Rev. B.* 33: 8800-8802.
72. Perdew J.P., Chevary J.A., Vosko S.H., Jackson K.A., Pederson M.R., Singh D.J., and Fiolhaus C. 1992. Atoms, molecules, solids, and surfaces: applications of generalized gradient approximation for exchange and correlation. *Phys. Rev. B.* 46: 6671-6687.
73. Barcaro, G.; Fortunelli, A.; Rossi, G.; Nita, F.; Ferrando, R. 2006. Electronic and structural shell closure in AgCu and AuCu nanoclusters. *J. Phys. Chem. B.* 110: 23197-23203.
74. Hansen J. P., and McDonald I. R. 1986. *Theory of simple liquids*. Academic Press. New York. p. 416.
75. Allen, M.P., and Tildesley D.J. 1987. *Computer simulation of liquids*. Oxford Science Publications. p. 385.
76. Itoh M., Kumar V., Adschiri T., and Kawazoe Y., eprint arXiv:0902.0080. 2009.

77. Pacheco-Contreras R. Energy Landscape Bimetallic Nanoparticles (Thesis). University of Sonora. 2010.
78. Ramli Ismail and Roy L. Johnston. 2010. Investigation of the structures and chemical ordering of small Pd–Au clusters as a function of composition and potential parameterisation. *Phys. Chem. Chem. Phys.* DOI: 10.1039/c004044d.
79. Andrew J. Logsdail, Z. Y. Li and Roy L. Johnston. 2012. Investigation of the Structures and Chemical Ordering of Small Pd-Au Clusters as a Function of Composition and Potential Parameterisation. *J. Comp. Chem.* DOI 10.1002/jcc.21976
80. Z. Y. Li et al. 2008. Three-dimensional atomic-scale structure of size-selected gold nanoclusters. *Nature*. Vol 451 pp. 46-49
81. <http://www.bear.bham.ac.uk>. Accessed on July 2010.
82. G. Rossi and R. Ferrando. Searching for low-energy structures of nanoparticles: a comparison of different methods and algorithms. *J. Phys.: Condens. Matter* 21 (2009) 084208 (11pp).
83. N. Dugan and S. Erkoc. Genetic Algorithms in Application to the Geometry Optimization of Nanoparticles. *Algorithms* 2009, 2, 410-428; doi:10.3390/a2010410.
84. R. H. Leary. Global Optimization on Funneling Landscapes. *Journal of Global optimization*. Vol. 18, Num. 4 (2000), 367-383, DOI: 10.1023/A:1026500301312